



Distributions of earth pressure and soil resistance on full buried single-row anti-sliding piles in loess slopes in northern Shaanxi based on in-situ model testing

Zhe Li¹ · Zhenguo Zhu² · Lulu Liu^{3,4} · Lei Sun¹

Received: 6 July 2021 / Accepted: 4 January 2022 / Published online: 1 March 2022
© Springer-Verlag GmbH Germany, part of Springer Nature 2022

Abstracts

Anti-sliding piles play a key role in slope stabilization. This study explored the distributions of earth pressure and soil resistance acting on full buried single-row anti-sliding piles installed in loess slopes. Two groups of in-situ model tests were carried out at a loess slope in northern Shaanxi, China, to observe the load transmission process between the loess and piles. Numerical simulations were used for auxiliary analysis. The in situ testing showed that the model piles failed by fracture damage. The distribution curve of earth pressure was parabolic, while that of soil resistance was shaped like an inverted trapezoid. The simulations showed similar distributions, illustrating that earth pressures have similar distributions under various embedded conditions and are related to the slip bed material and embedded depth, and soil resistance. Combining the results of the in situ tests and simulations, the axes of symmetry were predominately located at 1/3 of the load-bearing segment. The resultant force of earth pressure was located within the range of 9/16 to 3/5 of the load-bearing segment, while that of soil resistance was located at 3/10 to 2/5. These results demonstrate the distributions of earth pressure and soil resistance acting on full buried single-row anti-sliding piles installed in loess slopes that have a potential sliding surface. The results of this study will aid in anti-sliding pile design.

Keywords Anti-sliding pile · Loess slope · In-situ test · Earth pressure · Soil resistance · Distribution function

Introduction

The deformation and stability characteristics of retaining structures built on loess slopes have a major influence on the safety of adjacent built structures (Zhou et al. 2020). Anti-sliding piles are a type of retaining structure that has been widely used in slopes, especially loess slopes. A large number of studies have focused on the interactions between

anti-sliding piles and soil in recent years, such as Zhang et al. (2017) and Chen et al. (2020). However, because these piles are hidden in the ground, it difficult to identify the stress states that may influence them.

In recent years, a number of highways have been built in northern Shaanxi, a loess area in northwest China. Many artificial loess slopes reinforced by single-row anti-slide piles remained after road construction was completed. Follow-up monitoring observed that some anti-sliding piles had small but continuous horizontal displacements at the pile-top. Such problematic anti-sliding piles present an opportunity to study pile-soil interactions and load transmission processes so that pile design and use can be improved.

In a case study, Vassallo et al. (2019) reported on an interaction between a slow-moving landslide of clay soil and a railway tunnel protected by sheet pile walls that crossed the area of landslide accumulation. The results provide a basis for studying the interactions between multiple structures and soil. Inspired by previous methods, Li et al. (2015) and Li et al. (2017) used the finite element method in ANSYS software to apply a distributed load of earth pressure on the side

✉ Zhenguo Zhu
894420471@qq.com

¹ School of Highway, Chang'an University, Xi'an 710054, China

² School of Resource and Civil Engineering, Northeastern University, Shenyang 110819, China

³ Institute of Geotechnical Engineering, School of Transportation, Southeast University, Nanjing 211189, China

⁴ School of Engineering, University of Warwick, Coventry CV4 7AL, UK

of a 2D pile, rather than a load of soil along the pile, which is more common. Then, the deformation control principle was used to search for the failure criteria of anti-sliding piles. Some signs suggest that the pile-soil interaction process and deformation of pile are impacted upon the distribution of lateral stress. Thus, the distribution functions of earth pressure and soil resistance are the key focus of this study.

Designers have used the elastic foundation coefficient method to calculate the internal forces in anti-slide piles as it has a simple calculation process. Architects use a basic principle in anti-sliding pile design, which assumes that the embedded section below the sliding surface is like a beam on elastic foundation. The earth pressure and soil resistance on the sides of anti-slide piles are always assumed to have a triangular distribution. However, this assumption is overly simplistic for clayey soil. Some researchers have studied the distribution of earth pressure by numerical analysis (Zhou et al. 2014) and scale model testing (Tang et al. 2014), finding it to be parabolic. Dai summarized the distribution of earth pressure and soil resistance and derived distribution functions for different soil conditions (Dai 2002), including rock, sand, clay and sand-clay. Although the distribution of earth pressure has been studied for a long time, there has been little study of the distributions of earth pressure and soil resistance in loess slopes.

Landslides in loess slopes in northern Shaanxi can be divided into three categories: landslides in loess, red clay contact landslides, and bedrock contact landslides (Qiu et al. 2017). To simulate pile-soil interactions, researchers have carried out a number of laboratory model tests. Liu et al. (2011) designed a loess slope model of with single-row cantilever anti-sliding piles. Both the slipping mass and sliding bed were made of remoulded loess, while the sliding surface was a layer of plastic film. Other researchers have used various methods to imitate the pile-soil interaction process (Fan et al. 2019; Hull 1995; Li et al. 2016; Ozcelik and Yildirim 2014; Qian et al. 2011; Wang and Zhang 2013; Wang et al. 2017). However, the degree of influence on remolded soils remains unclear, especially for loess. Several studies have conducted in situ tests on anti-slide piles. Zomorodian and Dehghan (2011) conducted small-scale model tests to evaluate the lateral resistance of a single pile located near a reinforced sandy slope. Frank and Pouget (2008) conducted long-term tests to determine long-duration P–y lateral reaction curves. Kang et al. (2009) studied a large-scale cut slope subjected to staged reinforcement and investigated changes in its stability using field monitoring and slope modelling. Nimityongskul et al. (2018) carried out a series of full-scale lateral load tests of fully instrumented piles in cohesive soils their lateral responses in free-field and near-slope conditions. Smethurst and Powrie (2007) monitored a number of discrete piles used to stabilise a railway embankment at Hildenborough, Kent, UK. Song et al. (2012), However, laboratory tests remain relatively few. Another effective

method of studying pile-soil interactions is numerical analysis. Due to its simplicity, a large amount of work has been done by this method (He et al. 2018; Ho 2015; Hou et al. 2015; Li et al. 2012, 2013; Xiao 2016).

In recent years, it has become common to combine physical testing with numerical analysis to solve engineering problems. Liu et al. (2018) carried out laboratory model tests and imitated them in ABAQUS software to study h-type anti-slide piles. Lirer (2012) analyzed a slope with piles using long-term testing data and numerical analysis results. Lirer (2012) interpreted data from inclinometers placed upslope, downslope and along a pile to determine whether a plastic hinge formed. A similar method was used by Gu et al. (2014).

In the present study, to avoid effects between undisturbed and remolded loess (Xu and Guo 2020), in situ tests of pile models were conducted on a loess slope located along the G65w Highway, with undisturbed loess used as the soil around the piles. Then, a number of numerical tests were conducted to simulate the in-situ model tests. The aims were to understand (1) the loading transfer variation, (2) the failure mode of the anti-sliding piles, and (3) the distribution forms of the earth pressure and soil resistance on the piles' sides. These results were used to deduce a reasonable stress distribution function suitable for loess slope in northern Shaanxi.

In-situ model tests

General engineering situation

Prototype single-row anti-sliding piles were fully buried at an artificial loess slope toe located along the G65w Highway in northern Shaanxi, China. The lower two-thirds of each pile was embedded in sandstone. The piles were made of reinforced concrete (C30) with rectangular Sects. (2 m × 3 m) and lengths of 25 ~ 40 m, and were installed with a 6-m pile spacing. The reinforcement ratio in the tension area was 0.4% and the effective diameter was 64 mm. The landslide mass was mainly composed of Q₂ loess (average silt content about 82%). The sliding bed was sandstone and between the landslide mass and sandstone was a mudstone interlayer in local regions. The inclination angle of the slip surface ranged from 5° to 10° (Fig. 1).

Model scale choice

The linear scale determines the similarity in shape and size between a prototype and a model. In this study, the size of each prototype anti-sliding pile was length × width × height = 3 m × 2 m × 40 m, so the linear scale for

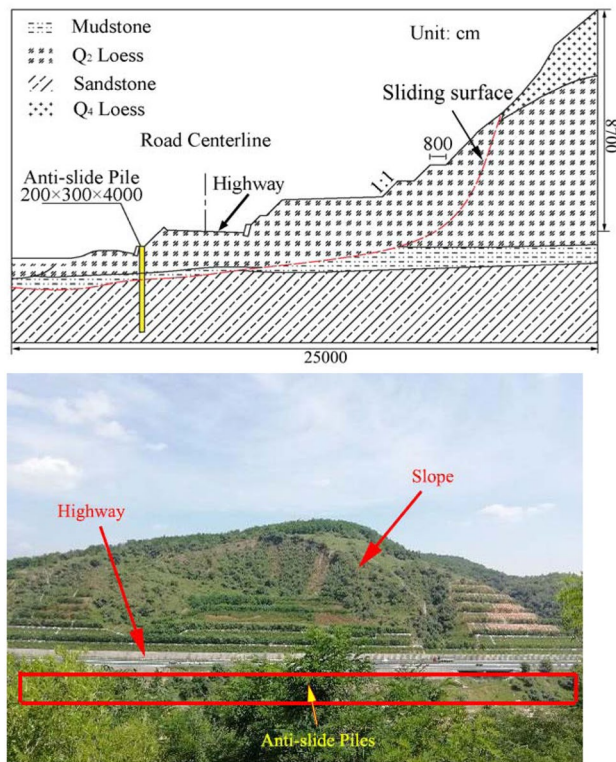


Fig. 1 Prototype slope and anti-slide pile along the highway in northern Shaanxi

the in-situ model tests was designated as 1:40, so that the model piles could be carried to the test site. In similarity theory, models are always made in a similar way to prototypes. Thus, the material, was selected in strict accordance with the linear scale but did not have enough strength for use in model piles. Many researchers have used other materials instead, such as stainless steel (Pan et al. 2002), a mixture of gypsum, sand and water (Wang and Zhang 2013), nylon (Li et al. 2016), aluminum pipe (Ozcelik and Yildirim 2014), and reinforced concrete (Liu et al. 2011, Qian et al. 2011, Tang et al. 2014). Most have used reinforced concrete as the model pile material and obtained reliable test results. Thus, in this study, the model pile material was C30 concrete with steel reinforcement. The corresponding physical variables were

$C_E = 1, C_\sigma = 1, C_\epsilon = 1, C_\rho = 1,$ and $C_q = 1 : 40,$ where E is the elastic modulus, σ and ϵ are the stress and strain in the anti-slide piles, respectively, ρ is the reinforcement ratio, and q is the loading on the pile sides. The parameters of the prototype and model piles are shown in Table 1. The top 5 cm areas of the model piles were used for displacement monitoring.

Designing of in-situ model test

Two groups of in-situ model tests were designed to explore the deformation process in single and double piles. Each test had several parts, including a loading system, force transmission system, monitoring system and reaction wall. Hydraulic jacks were used to apply horizontal and vertical loadings in the tests. The force transmission section was made of a sheared block 60 cm long x 60 cm wide x 33 cm high. The model anti-sliding piles were fully buried in undistributed loess in front of the shear blocks. Figure 2 shows the design of the in situ model tests.

Model pile prefabrication

Precast reinforced concrete piles were used in the model tests. Reinforcement cages of 8-mm diameter were made of hand-woven wire and placed inside the piles. The composition of the pile concrete was 1 water:2.1 concrete:4.2 sand:6.9 fine stone:1.2 admixtures. The whole process of pouring the model piles was conducted on a vibrating table to ensure good fabrication quality (Fig. 3a).

Sensor placement

Strain gauges and micro earth pressure cells were pasted onto the sides of the piles to monitor the bending moment, earth pressure and soil resistance (Fig. 3b and c).

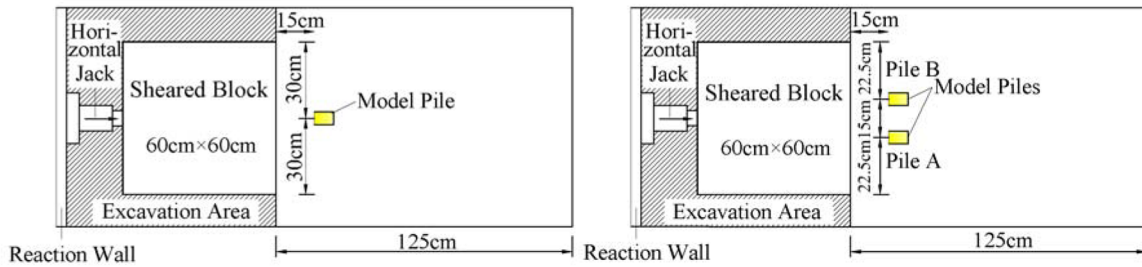
Test site

It was not possible to conduct the tests near the prototype anti-sliding piles, so a testing site was selected on a slope along the G65w Highway near the Wanhua Tunnel exit, which was not too far from the prototype piles. The artificial

Table 1 Parameters and materials of prototype and model anti-slide pile

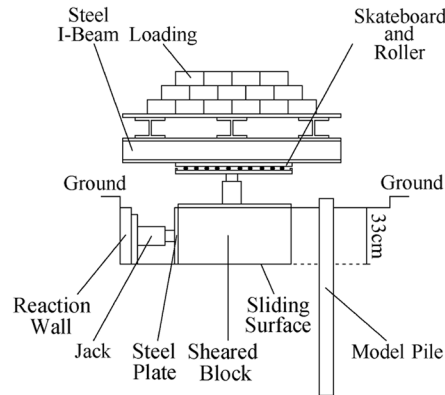
Type	Section size (width x length) (cm)	Pile length (cm)	Pile material	Reinforcement material	Reinforcement ratio (%)
Actual pile	200 x 300	4000	C30	HRB400 (effective diameter = 64 mm)	0.4
Model pile	5 x 7.5	105 (100 + 5)	C30	Steel wire (diameter = 1.6 mm)	0.4

The length of model pile should be 100 cm, the extra part will be used to observe displacement of pile top

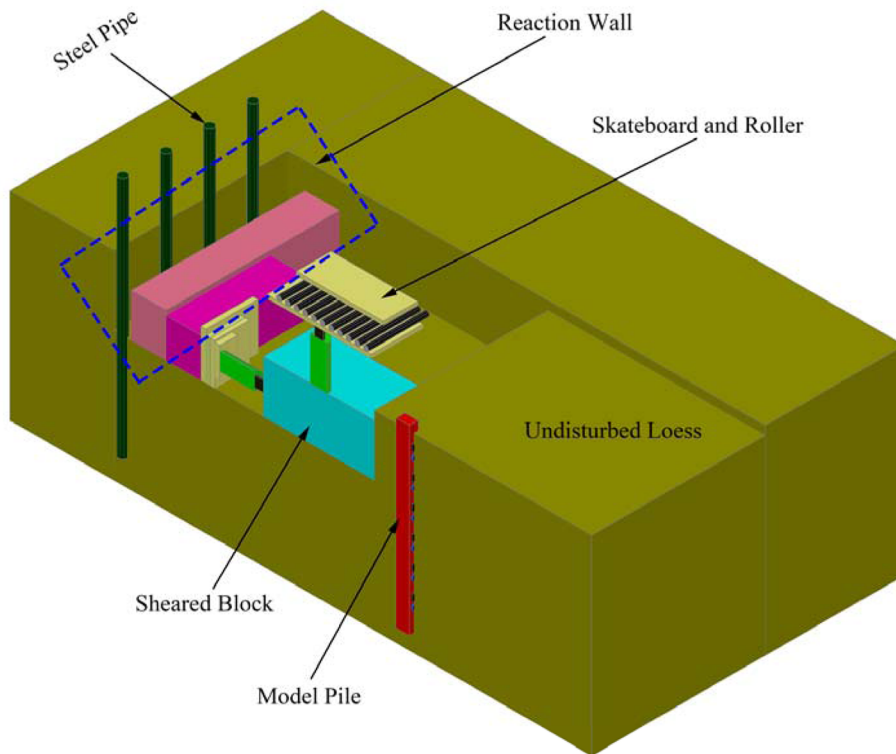


a. Designing of single pile

b. Designing of double piles



c. Test diagram of in-situ single-row anti-sliding pile model tests



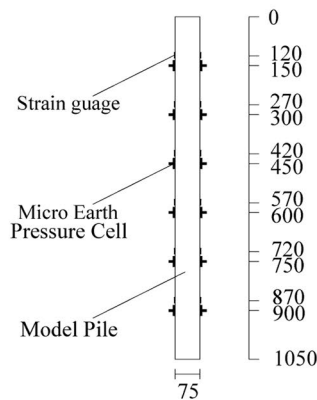
d. 3D sketch of in-situ model tests (single pile)

Fig. 2 Designing of in-situ single-row anti-sliding pile model tests. **a** Designing of single pile. **b** Designing of double piles. **c** Test diagram of in situ single-row anti-sliding pile model tests. **d** 3D sketch of in situ single-row anti-sliding pile model tests (single pile)

slope was over 130 m high and was named Wanhua Slope. It had 14 steps and a gradient ranging from 1:1 to 1:0.5. There was a 20-m-wide platform at the fourth step, which



a. Pouring model piles on the miniature vibration table



b. Placement of sensors on the model pile sides (unit: mm)



c. The model pile with sensors

Fig. 3 Manufacturing and sensor layout of model piles. **a** Pouring model piles on the miniature vibration table. **b** Placement of sensors on the model pile sides (unit: mm). **c** The model pile with sensors

had enough area to conduct the in-situ model tests. The location of testing site is shown in Fig. 4.

Test details

Some key factors that needed to be controlled in the tests were the pile holes, embedding conditions and sheared blocks.

It is critical that precast model piles are placed perfectly in the designed position. In this study, a Luoyang shovel with a rectangular section measuring 6 cm long × 9 cm wide was custom-made to make the holes required for the model tests (Fig. 5c).

In order to enhance the strength of the lower soil, some cement was poured into the holes to replace the subsoil after meeting the elevation requirement. The model piles did not make close contact with the surrounding soil due to measurement discrepancy between the piles and holes. Model piles were wrapped with multiple layers of plastic film to isolate them from soil water. Thus, a certain amount of cement soil, consisting of cement, water and loess, was infused into the interspaces to enhance contact between then model piles and soil.

Before the model tests, the sheared blocks needed to be pretreated. The size of the sheared blocks was 60 cm width × 60 cm length × 30 cm high, and they were designed according to the in situ direct shearing tests. A shear box (60 cm wide × 60 cm long × 30 cm high) was produced following the regulations for in situ direct shear tests. However, there were some differences during their preparation. Shear blocks were excavated at the test site. At first, the upper surfaces and three free surfaces of the sheared blocks were cut and flattened to the designed sizes. The last surface was placed near the model piles. Then, for security during the consolidation process, a slot of 60 cm × 3 cm × 30 cm was carved between the sheared block and the soil around the pile. A steel plate was put in the slot to provide absolute lateral confined constraints during vertical consolidation of the soil blocks and prevent them from collapsing. After vertical consolidation, the steel plate was removed and the slot was filled with compacted soil.

Loading method

The purpose of the in-situ model tests was to simulate the landslides process, including slippage, extrusion on the pile sides, and transmission of lateral loads to the modelled pile-soil. Therefore, it was necessary that the sheared blocks could be compacted to simulate the real stress status. The consolidation pressure was 300 kPa, and it was reloaded as a normal loading when the testing started.

Fig. 4 Location of in situ single-row anti-sliding pile model test ground (in loess area in northwest China)



Lateral loading scheme: A jack was used to apply lateral design loads that increased from 0 kPa in 30 kPa steps. When the accumulated lateral load reached 120 kPa, the step size was adjusted to 10 kPa and the designed load was measured by a liquid-pressure gauge on the jack. The application of lateral load stopped when the increment in the horizontal displacement of the pile-tops was consistent with that of the soil blocks at multiple levels in succession or exceeded that of the sheared soil blocks.

Monitoring method

The horizontal and vertical placements of the pile-tops, the horizontal placement of the sheared soil blocks, the pressure and resistance of the soil beside the piles, and the bending moments of the piles needed to be monitored

during the model tests. The horizontal and vertical placements of the pile-tops were individually monitored by a 30 mm dial indicator, while the horizontal placements of sheared blocks were monitored by a 100 mm dial indicator. A strain collector collected data from each sensor at a frequency of 1 Hz regarding the pressure and resistance of the soil beside the piles and the pile bending moments.

Testing procedure

Photographs of the main components of the model testing process are shown in Fig. 5, where Fig. 5a shows the cutting and finishing of sheared blocks, Fig. 5b shows the installation of steel plates to form a shear box, Fig. 5c shows the making of pile holes, Fig. 5d shows the application of a

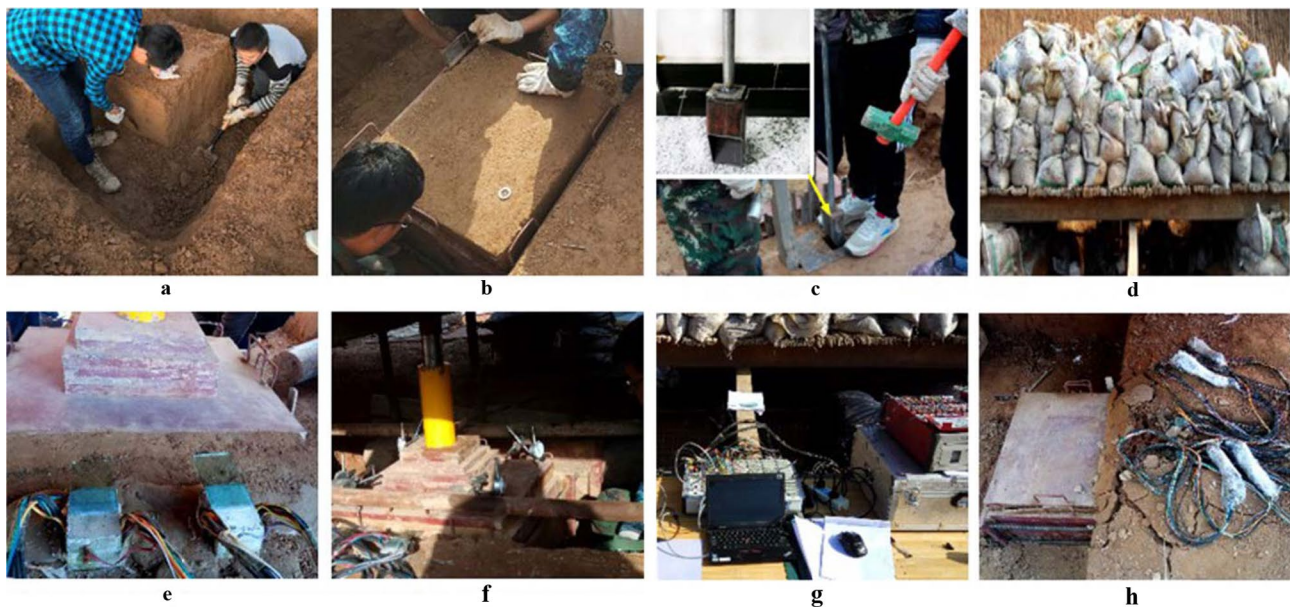


Fig. 5 The mainly process of model test, where **a** is excavating the shear block; **b** is installing the shear box; **c** is drilling into the model slope by a specially made Luoyang shovel; **d** is applying the normal

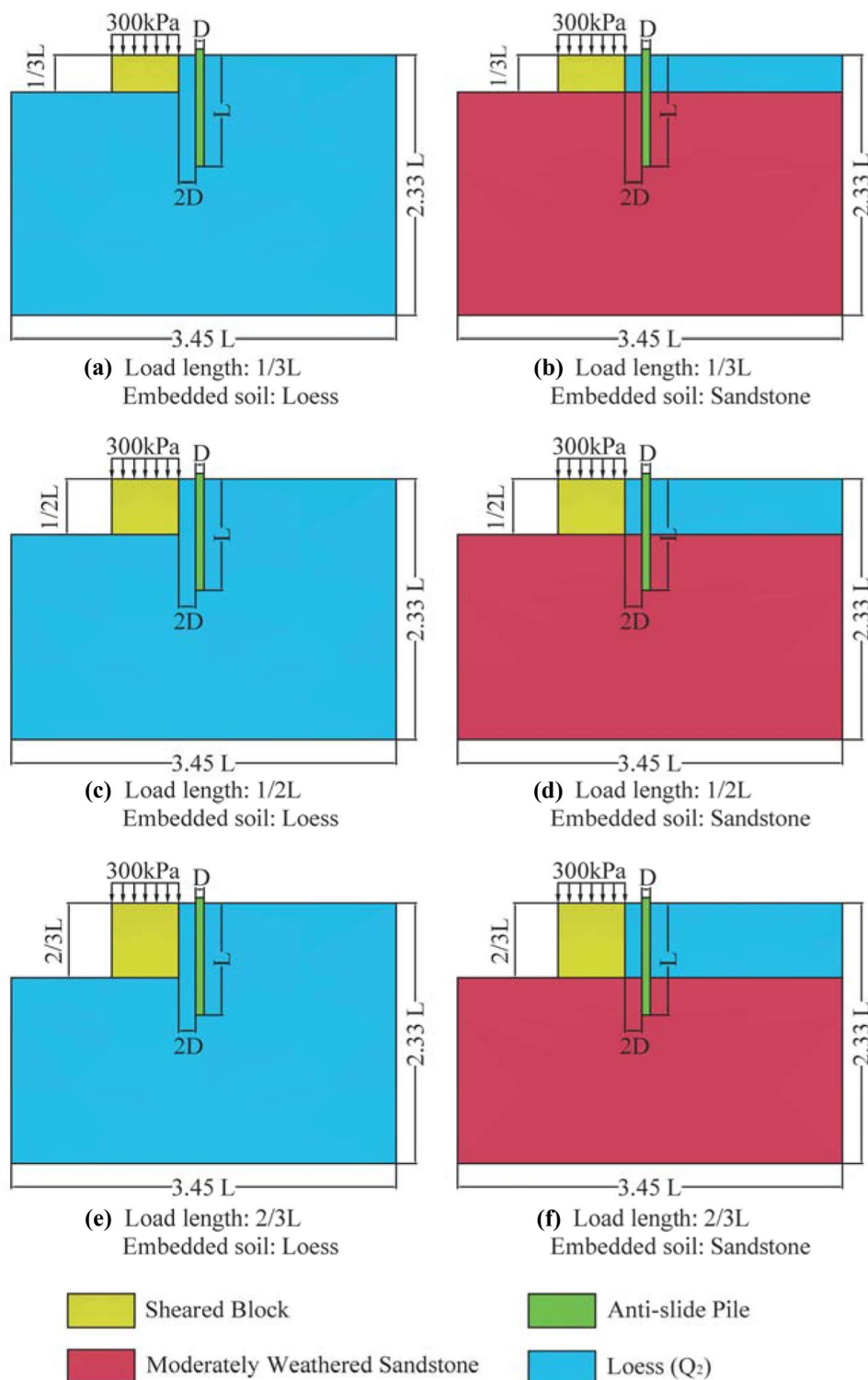
load; **e** is embedding model piles into undisturbed loess; **f** is the consolidation process under 300 kPa normal load; **g** is the instrument; **h** is the overview of piles and shear block after the test

normal load, Fig. 5e shows the placement of model piles into pile holes and infusion with cement-soil grout, Fig. 5f is sticking glass capable on the top of model pile, Fig. 5g shows the process of consolidation, Fig. 5h shows the commissioning of instruments before the tests, and Fig. 5i shows the state after testing.

Numerical testing based on in-situ model tests

In situ model testing can provide information about pile-soil interactions on loess slopes but has some limitations. For example, full-scale tests are difficult to carry out due

Fig. 6 Numerical test designing (the control variable contains load length and embedded condition)



to their size and only some of the boundary conditions can be simulated. Therefore, based on the in-situ model tests, numerical analysis was used as another way to explore the pile-soil interactions.

Numerical test designing

Three conditions were controlled in the numerical tests: the embedded condition, embedded ratio, and number of anti-slide piles. The embedded conditions comprised Q_2 loess and moderately weathered sandstone because the model piles were embedded in Q_2 loess while the prototype piles were embedded in moderately-weathered sandstone. Hence, the degree of impact of the embedding conditions on the earth pressure and soil resistance relationship could be determined.

The embedded ratio is a parameter that describes the length of embedded segments. In the numerical tests, the embedded ratios included $2/3$, $1/2$, and $1/3$, which are commonly used values in anti-slide pile design. These variables can determine whether the relationship between earth pressure and soil resistance varies according to embedded depth.

The last condition controlled in the tests was the number of piles. Single, double, and triple piles were used to determine the effect of pile number on the relationship between earth pressure and soil resistance.

Schematics of the test designs are shown in Fig. 6, which shows the single-, double-, and triple-pile conditions used for the numerical analyses. A total of 18 tests was conducted in ABAQUS. All the dimensions used in the numerical models were consistent with those of the in-situ model tests (Fig. 7).

Numerical model parameters

The main parameters of the numerical model are shown in Table 2. The Mohr–Coulomb model was adopted for undisturbed loess and sheared blocks, and the unit type was C3D8R. The CDP concrete model was adopted for the C30 concrete, and the unit type was C3D8R. The plastic model was adopted for the reinforcement cages and the unit type was T3D2.

Loading method

A displacement loading method was used to apply lateral loads in the tests by step-by-step horizontal displacement of the rear of the sheared blocks based on the displacements observed in the in situ model tests. The displacement loads in each step are shown in Table 3.

Results and discussion

In-situ model test results

Displacement result analysis

The horizontal and vertical displacements of the pile-tops obtained from the in-situ model tests are shown in Fig. 8, of which horizontal displacements were greater. The increase in horizontal displacement was more rapid in single piles than double piles.

A comparison of the horizontal displacement curves of the pile-tops and sheared blocks is shown in Fig. 9a. Unlike the horizontal displacement of pile-tops and

Fig. 7 Numerical model (as a sample, the model of single pile test is shown in Fig. 7)

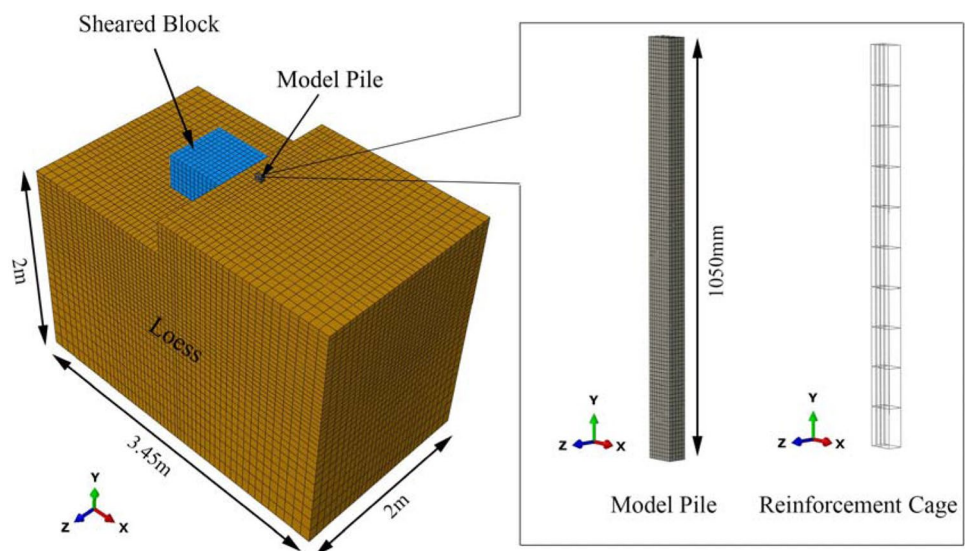


Table 2 Main parameters of material

	ρ (kg/m ³)	E (Pa)	ν	c (Pa)	ψ (°)
C30	2380	3×10^{10}	0.25	-	-
Undisturbed loess	1720	3.3×10^7	0.35	3.3×10^4	29
Shear block	1800	4×10^7	0.35	3.7×10^4	31
Reinforcement caging	7850	2.1×10^{11}	0.25	-	-

sheared blocks, the stress deformation process in the model anti-slide piles had three stages: non-deformation, effective deformation and failure. The boundary between the first and second stages was named as *critical start-up load*, i.e., the horizontal load when the model pile began to deform. The boundary between the second and third stages was named as *critical stabilizing load*, i.e., the maximum horizontal load that the model pile could resist.

The critical start-up load was the lateral load when a horizontal displacement first occurred at pile-top. It was determined from the curve of displacement increasement at the pile-top. To determine the critical stabilizing load, the key was to compare the horizontal displacement increments of the shear block and pile top. This is because, with the development of lateral load, the displacement increment at the pile-top becomes closer to that of the shear block if a fracture has occurred in the pile body. Thus, we selected the boundary which horizontal displacement at the pile-top started to decrease at the next load stage compared with the difference of horizontal displacement of the sheared block as the critical stabilizing load.

The results of the above division method are shown in Fig. 9b. The critical start-up loads were 43 kN for single piles and 32.5 kN and 22 kN for the double piles A and B, respectively. The critical stabilizing load of single piles was 89.5 kN, while double piles A and B had the same critical value of 93 kN. Comparing the two model tests, double piles had a longer effective deformation state and a higher critical stabilizing load. However, piles A and B had different critical start-up loads, which could indicate that they had different stress states in the system.

Earth pressure and soil resistance results

The data measured by the miniature earth pressure cells were substituted into Eq. (1) to calculate the earth pressure and soil resistance.

Table 3 The displacement loading in different steps

Step time	0	0.05	0.1	0.15	0.2	0.25	0.3	0.35	0.4	0.45	0.5
Displacement (mm)	0	0.05	0.09	0.102	0.243	0.489	0.826	1.258	1.576	1.978	2.483
Step time	0.55	0.6	0.65	0.7	0.75	0.8	0.85	0.9	0.95	1.0	-
Displacement (mm)	3.723	4.917	6.472	7.378	8.52	9.732	11.506	12.77	14.165	14.983	

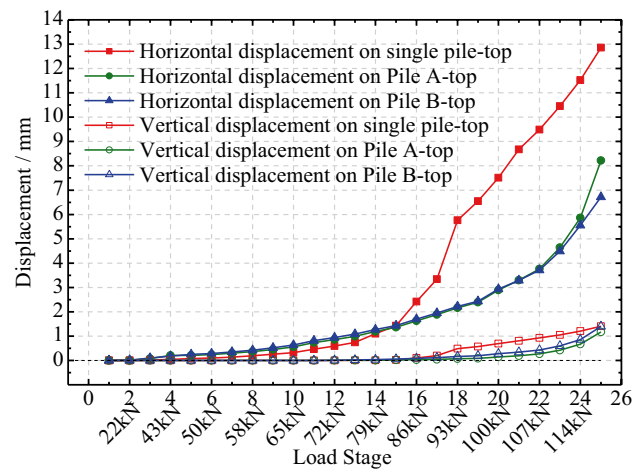


Fig. 8 Horizontal and vertical displacement of pile-top

$$Y = \frac{X - A}{10K} \times 10^3 \tag{1}$$

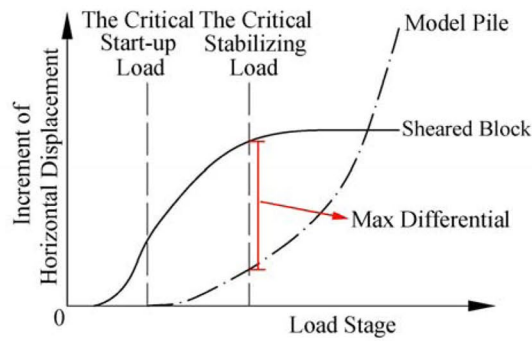
where Y is earth pressure or soil resistance (kPa); X is the strain measured by the pressure boxes; A is the strain value corresponding to a pressure meter reading of 0 kPa according to the calibration parameter table; and K is a sensitivity coefficient corresponding to each pressure box.

The variations in earth pressure and soil resistance on the sides of a single pile are shown in Fig. 10a. The figure shows that with increasing lateral load, both earth pressure and soil resistance increased consistently from the 1st to 17th load stages. The variation in earth pressure first increased and then decreased with increasing depth and the maximum possible earth pressure was near the sliding surface. However, soil resistance decreased as depth increased, and there was hardly any soil resistance under the sliding surface on the sides of the model pile. After the 18th stage of loading, the variations in earth pressure and soil resistance changed significantly; the earth pressure increased sharply, which is a signal of damage.

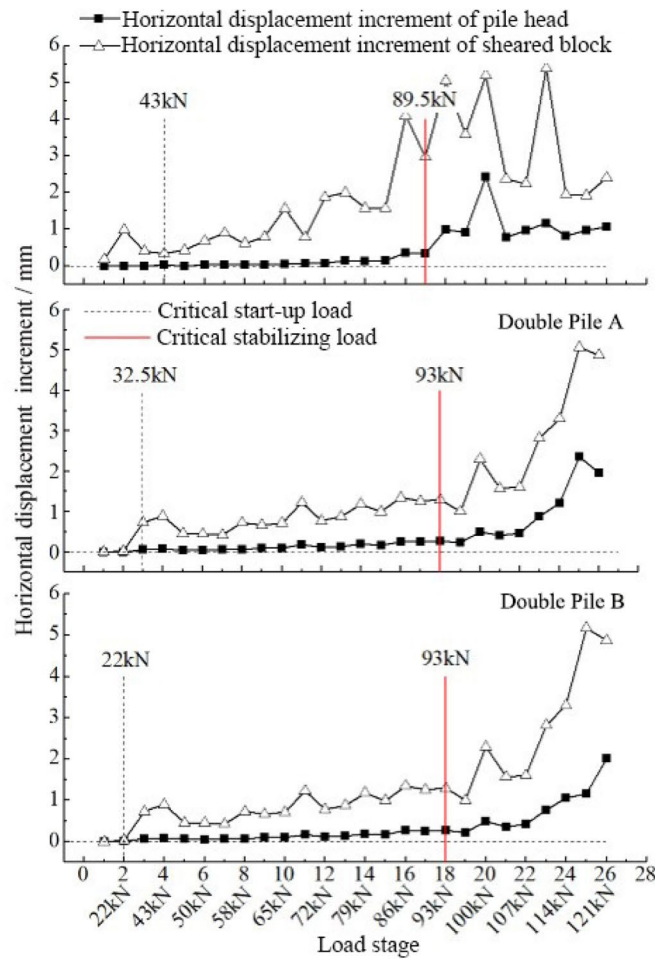
The variations in earth pressure and soil resistance on the sides of double piles A and B with increasing load are shown in Fig. 10b and c.

With increases in lateral load, the earth pressure on the sides of double piles A and B varied in a similar way as that of single piles. The pressure below the sliding surface decreased gradually to zero with increases in depth. However, the soil resistance was considerably greater than with single piles and

Fig. 9 Partitioning method of stress states of anti-slide pile. **a** Horizontal displacement increment relation curve between pile-top and sheared block. **b** Horizontal displacement increment on pile-top and sheared block



a. Horizontal displacement increment relation curve between pile-top and sheared block

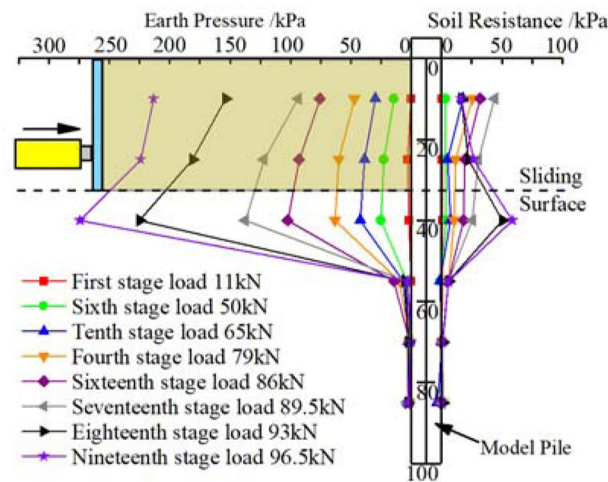


b. Horizontal displacement increment on pile-top and sheared block

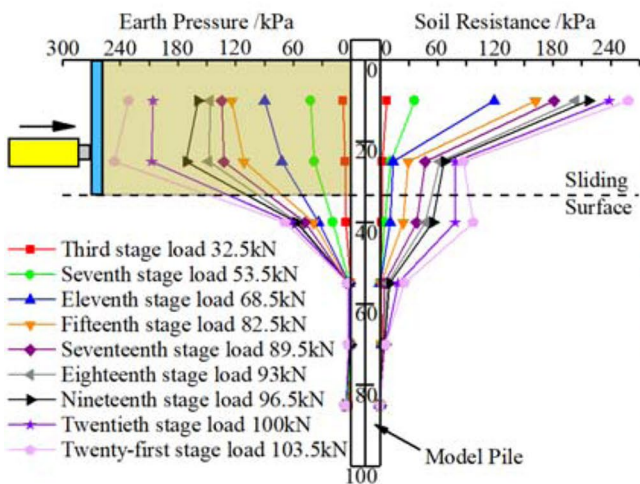
decreased with depth. After accumulating a certain amount of deformation (18th stage), the distributions of earth pressure and soil resistance began to change to a certain extent; pile A had a greater amount of change than pile B.

Bending moment

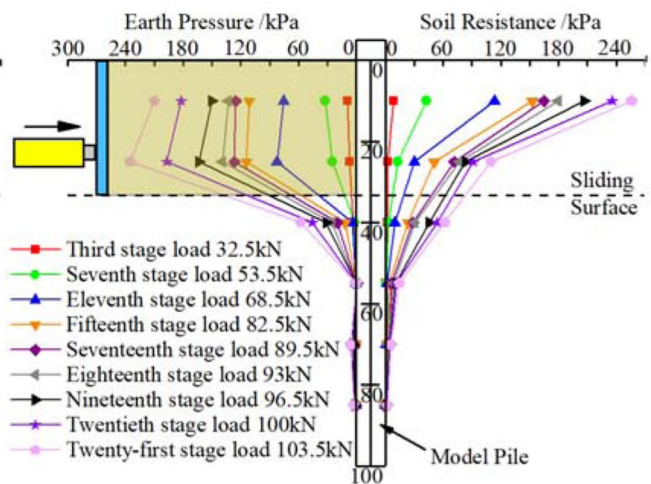
The data measured by the strain gauges were substituted into Eq. (2) to calculate the bending moment.



a. Single pile



b. Double Piles (A)



c. Double Piles (B)

Fig. 10 Variation curves of earth pressure and soil resistance on the pile sides. a Single pile. b Double piles (A). c Double piles (B)

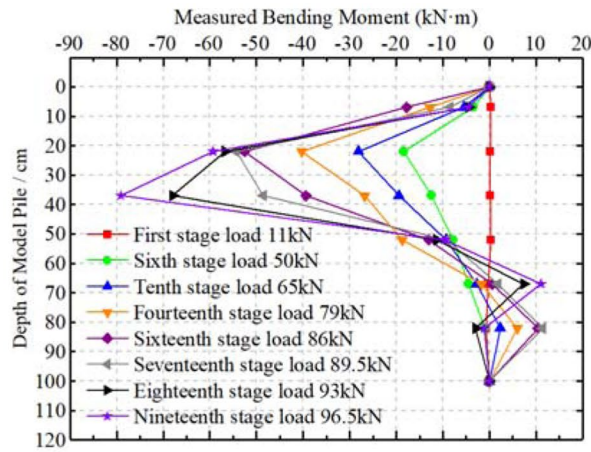
$$M = EI\Delta\epsilon/B \tag{2}$$

where M is the bending moment of the shaft of the model piles; E is the elastic modulus of the model pile shaft material; I is the sectional inertial moment of the model pile; and B is the distance between the strain gauges in the stress and compression zones of the model pile shafts.

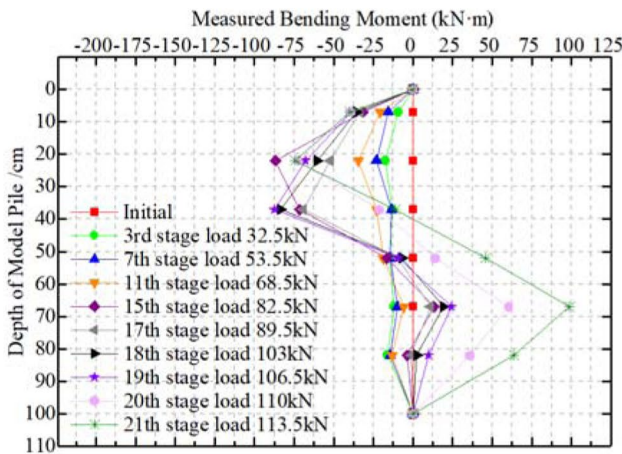
Bending moment curves of the single pile under different lateral loads are shown in Fig. 11a. It shows that in the first two stages (non-deformation and effective deformation), the curves are approximately S-shaped

with increases in lateral load. The initial measurement point of the maximum bending moment was located at a depth of 22 cm. After the 18th load cycle, the bending moment curve was redistributed and the maximum point was shifted to 37 cm.

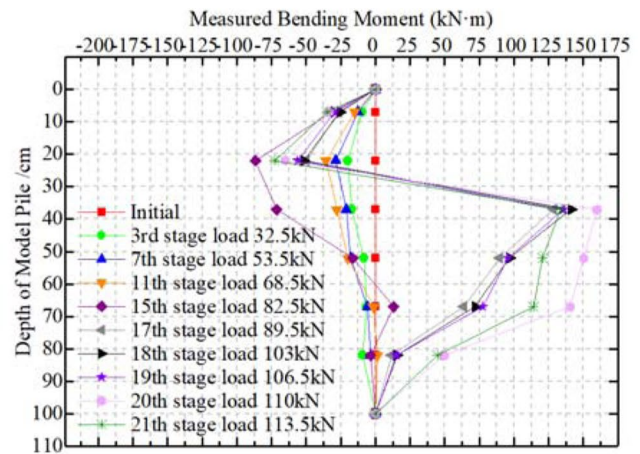
The bending moment curves of the double piles under different lateral loads are shown in Fig. 11b and c. They show that during the loading process, the bending moments of double piles A and B gradually changed from an approximate spoon-shape to an approximate S-shape. Comparing the bending moments of double piles A and B, it can be



a. Single pile



b. Double Piles (A)



c. Double Piles (B)

Fig. 11 Variation curves of bending moment of model piles. a Single pile. b Double piles (A). c Double piles (B)

seen that the bending moment of double pile B had an earlier redistribution and a larger extent of change.

Significantly, in the test of double piles, the displacement increment of double piles A and B showed a tendency for alternating increases under various lateral load, as demonstrated in Fig. 9b, as did their bending moments. This phenomenon suggests that the two piles had a continual stress redistribution process under the lateral load. When lateral load was transferred to the piles by the loess, an intercoordination process between the two piles was apparent. Double pile A was the first component to suffer fracture failure because of the greater lateral displacement increment, greater earth pressure and greater bending moment during load stage 19 (the critical stabilizing load) based on previous results.

Failure mode of model piles

After finishing the two groups of model tests, the broken piles were dug out. All model piles exhibited fracture damage, some with two damage points. Figure 12 shows the failure mode of the model piles.

The failure modes of the single-row anti-sliding piles could be classified as overturn and fracture failure. Under the embedded and boundary condition of the prototype structure, the piles had a greater probability of fracture. This indicates that the force–deformation process observed in the in-situ scale model tests successfully simulated the basic fracture failure mode of single-row anti-slide piles under the embedded conditions. A similar failure mode was achieved as reported in Liu et al. (2011) and Li et al. (2016).

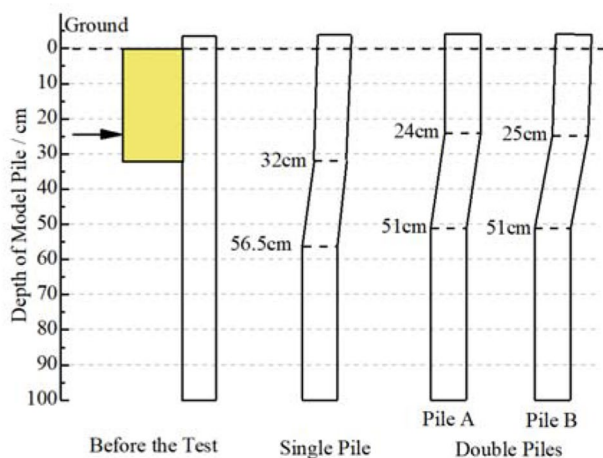


Fig. 12 Failure shape of model piles obtained by in situ model tests (both the single pile and double piles have two breaking-down point, but the single pile has a deeper breaking-down point)

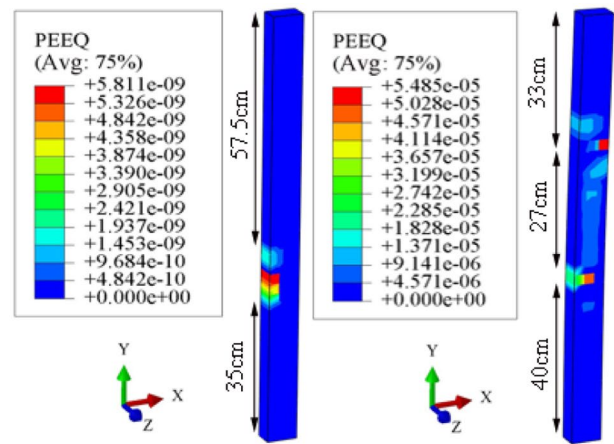
Comparing with laboratory model test, the in situ model tests designed in this paper have two advantages: (1) they used undisturbed loess soil around the piles to avoid the influence of the structural difference between undisturbed loess and remoulded compacted loess; (2) the slope's gravity was simulated by using a shear block as a lateral load transmission mass, which maintained a normal load of 300 kPa during the shearing process.

There are also some deficiencies in the tests; for instance, the gravity of piles was not simulated reasonably. However, anti-slide piles are non-vertical-bearing and aim to resist lateral thrust. The gravity of the piles and the lateral friction on their sides have less influence on their lateral stress response than lateral load. Moreover, inevitably, scale model tests are also affected by the specimen size. Due to the small size of the model piles, the compressive and tensile strengths of the concrete they were made from were lower than those of actual piles, which could cause earlier fracture. However, the failure behaviors of the concrete (brittle fracture) and reinforcement (tensile failure) were the same as those of actual structures. Thus, the in-situ model tests could adequately demonstrate the basic load transmission process between the loess and piles and the failure mode of single-row anti-slide piles.

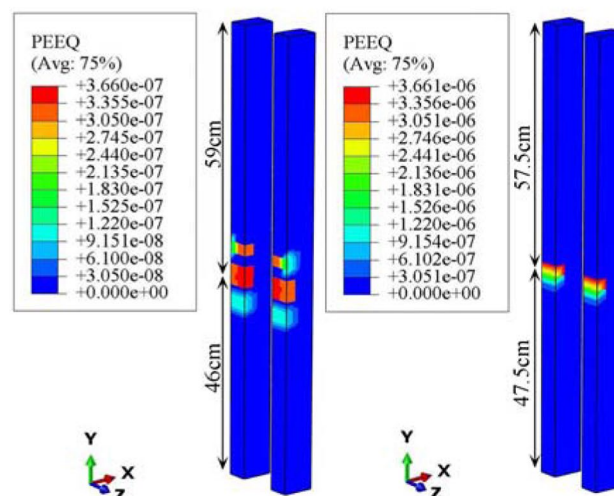
Numerical test results

Failure mode of the piles in numerical testing

We wanted to test whether the numerical tests approximated real pile-soil interactions. The simplest method was to compare the failure modes of piles in the numerical and



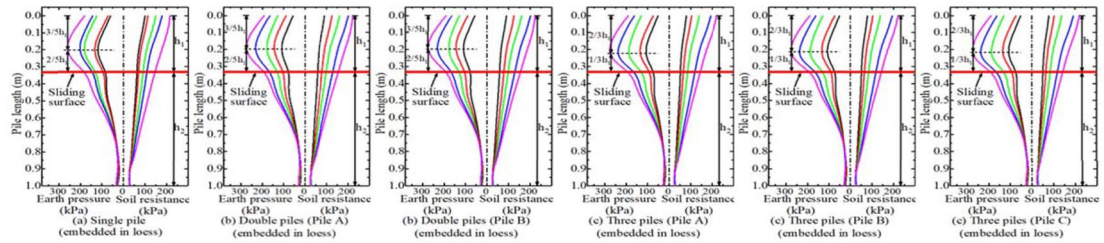
a. Single pile



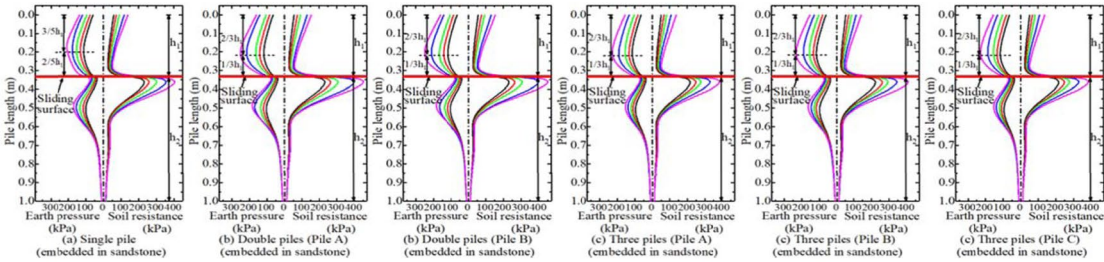
b. Double piles

Fig. 13 Damage evolution process of piles obtained by numerical tests. **a** Single pile. **b** Double piles

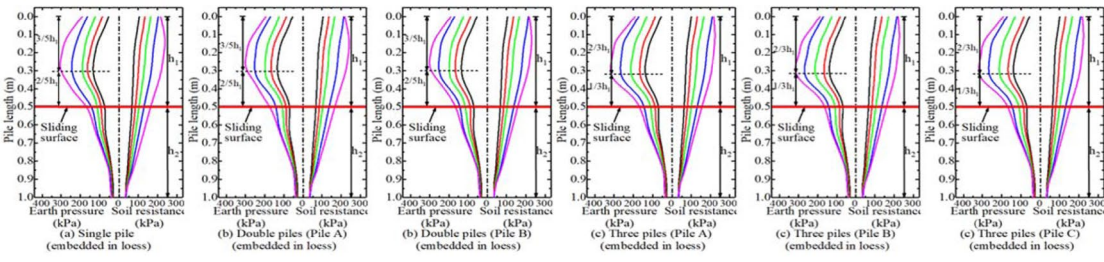
in-situ model tests. Figure 13 shows the pile damage process according to numerical testing, which had the same boundary conditions as the two groups of in-situ model tests. The figure shows that the pile damage points obtained by numerical testing mainly started at about two-thirds of the pile height. With increasing lateral displacement behind the sheared block, another damage point occurred at about one-third of the pile height, which had an opposing direction to that observed in the single-pile test but not in the test of double-pile tests. The most likely reason is that double piles had stronger resistance than single piles under the same lateral displacement condition. The damage mode obtained by numerical testing showed a similar process to that observed in the in situ model tests, which indicates that the numerical tests were credible.



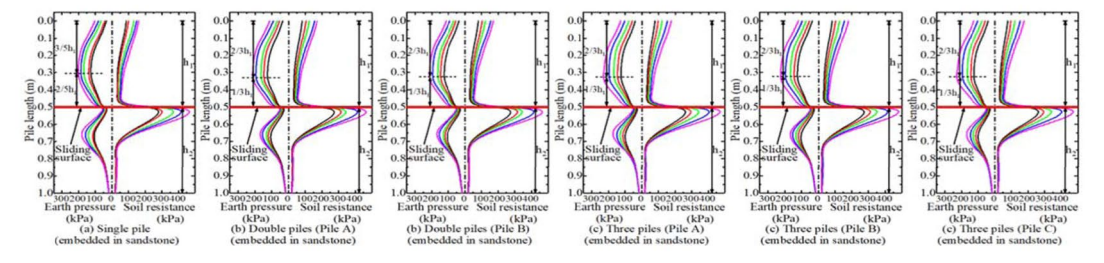
a. Earth pressure and soil resistance on the sides of pile under the condition of Figure. 6a



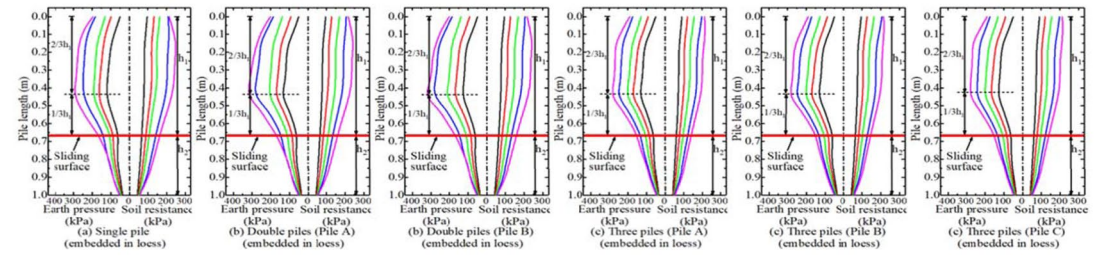
b. Earth pressure and soil resistance on the sides of pile under the condition of Figure. 6b



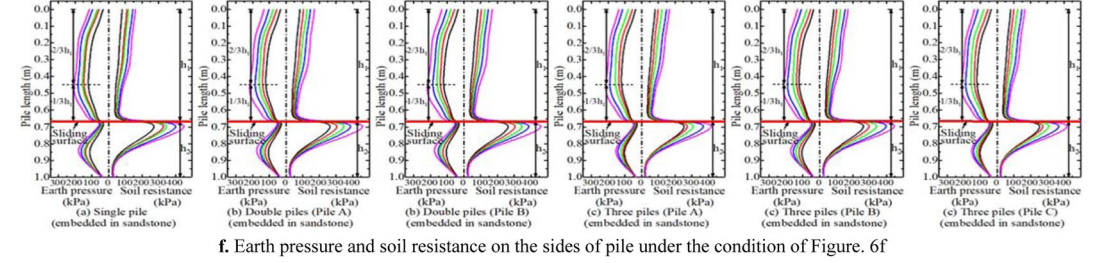
c. Earth pressure and soil resistance on the sides of pile under the condition of Figure. 6c



d. Earth pressure and soil resistance on the sides of pile under the condition of Figure. 6d



e. Earth pressure and soil resistance on the sides of pile under the condition of Figure. 6e



f. Earth pressure and soil resistance on the sides of pile under the condition of Figure. 6f

Fig. 14 Earth pressure and soil resistance on the sides of pile in different conditions obtained by numerical analysis. **a** Earth pressure and soil resistance on the sides of pile under the condition of Fig. 6a. **b** Earth pressure and soil resistance on the sides of pile under the condition of Fig. 6b. **c** Earth pressure and soil resistance on the sides of pile under the condition of Fig. 6c. **d** Earth pressure and soil resistance on the sides of pile under the condition of Fig. 6d. **e** Earth pressure and soil resistance on the sides of pile under the condition of Fig. 6e. **f** Earth pressure and soil resistance on the sides of pile under the condition of Fig. 6f

Soil pressure and soil resistance

The soil pressure and soil resistance values at the pile side at the initial phase of pressure (before or just after damage to the pile body occurred) obtained from numerical tests are plotted in Fig. 14. Figure 14a shows the results of soil pressure and soil resistance at the pile sides of all piles under the operating mode shown in Fig. 6a. Figure 14b shows the results corresponding to Fig. 6b. Figure 14c, d, e, and f show the results corresponding to Fig. 6c, d, e, and f, respectively.

As Fig. 14 shows, the earth pressure varied in an almost parabolic manner under all conditions. The parabola had a value > 0 at 0 m depth, which is different from the results achieved by Dai (2002). The location of the axis of symmetry of the landslide-thrust parabola mainly ranged from three-fifths to two-thirds of the depth of the loading section, with two-thirds being the most frequent result, especially under multiple-pile conditions. The soil resistance variation had an approximately inverted-trapezoid shape.

Derivation of earth pressure and soil resistance functions

Models of the variations in earth pressure and soil resistance were established according to the soil pressures and resistances measured on the pile sides during the in situ model tests and numerical tests.

Basic assumptions (1) The pile-side soil was treated as an elastic medium and the anti-sliding pile was treated as an elastic member; (2) the friction and adhesion of the pile-side soil and side of the anti-slide pile were ignored; (3) contact was maintained during the process; (4) the distribution of earth pressure was parabolic and that of the soil resistance was an inverted trapezoid. The models of earth pressure and soil resistance based on these assumptions are shown in Fig. 15.

Here, E is the value of landslide-thrust (earth pressure), and E' is the value of soil resistance; $q(z)$ is the distribution density of earth pressure with anti-sliding pile depth; $p(z)$ is the distribution density of the soil resistance with anti-sliding

pile depth; h_1 is the length of the anti-sliding pile above the sliding surface, h_2 is the length of the embedded section of the anti-sliding pile; z'_0 is the distance from the pile-top to the point of the resultant force of the earth pressure; z_0 is the distance from the pile-top to the point of the resultant force of the soil resistance; and k and k' represent the ratio between the height of the resultant force and the length of the loaded segment, where $z_0 = kh_1$ and $z'_0 = k'h_1$.

In the coordinate system, the lateral axis u expresses the horizontal displacement while the vertical axis z expresses depth. We define the arrow direction as the positive direction.

In brief, the derivation process was as follows. Suppose that a parabolic distribution function of earth pressure for a general case is:

$$q(z) = az^2 + bz + c \tag{3}$$

According to the formula of earth pressure:

$$\int_0^{h_1} (az^2 + bz + c) dz = E \tag{4}$$

$$\frac{1}{E} \int_0^{h_1} (az^2 + bz + c) z dz = kh_1 \tag{5}$$

According to the properties of the axis of symmetry:

$$z = -\frac{b}{2a} = nh_1 \tag{6}$$

where n is a proportionality factor describing the position of the axis of symmetry.

The parameters of the parabola are as follows:

$$a = \frac{(12k - 6)E}{(1 - 2n)h_1^3},$$

$$b = \frac{(12 - 24k)E}{(1 - 2n)h_1^2},$$

$$c = \frac{(1 - 2n)E + 2(3n - 1)(2k - 1)}{(1 - 2n)h_1}$$

In the case when $n=2/3$, the landslide-thrust distribution function is:

$$q(z) = \frac{(18 - 36k)E}{h_1^3} z^2 + \frac{(72k - 36)E}{h_1^2} z + \frac{E + (6 - 12k)}{h_1} \tag{7}$$

where the value of k is estimated according to the performance of the functional image and test results. The value of k ranges from 9/16 to 3/5, mostly closer to the latter.

The distribution function obtained in this study was the same as that of Dai (2002), so the function was given as follows:

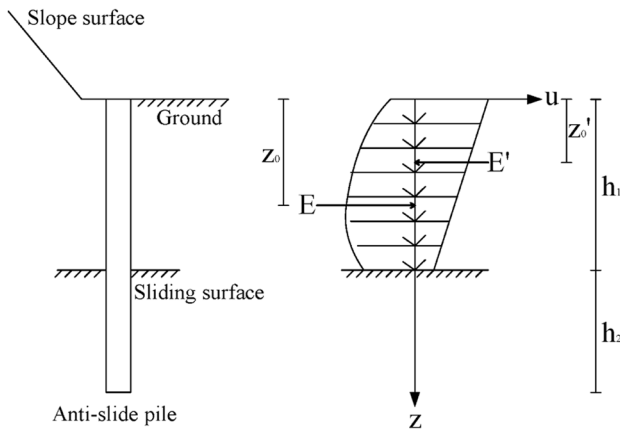


Fig. 15 Function model of landslide-thrust and soil resistance

$$p(z) = \frac{(12k' - 6)E'}{h_1^2}z + \frac{(4 - 6k')E'}{h_1^2} \quad (8)$$

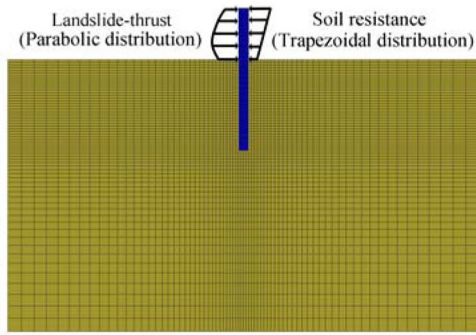
where the value of k' was determined according to the results of the in-situ model tests and numerical tests. The value is also consistent with the range reported by Dai (2002), which was 3/10 to 2/5.

Verification of function expression

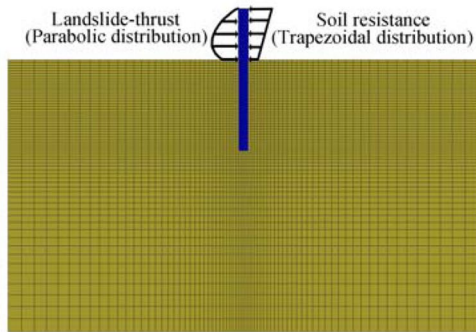
The distribution forms and functional expressions of earth pressure and soil resistance need to be verified before applying them to practical projects. The results achieved above show that change in the embedded condition of the model pile had almost no influence on the distribution forms of earth pressure and soil resistance at the pile sides. Therefore, verification with these results, which were obtained under the same conditions as the in-situ model tests, was considered sufficient.

A numerical method similar to that of Li et al. (2015) was used to verify the distribution function obtained in this study. The distribution functions of earth pressure and soil resistance obtained above were applied to the pile sides. To compare the results, three kinds of distributions were applied on the pile sides. They were based on the results of this study, the study of Dai (2002), who obtained a parabolic distribution earth pressure for clay and a triangular distribution of earth pressure (Fig. 16). It is worth noting that Dai's distribution function is a parabola over the pile top, while parabola that does not go through the pile top was obtained by present study.

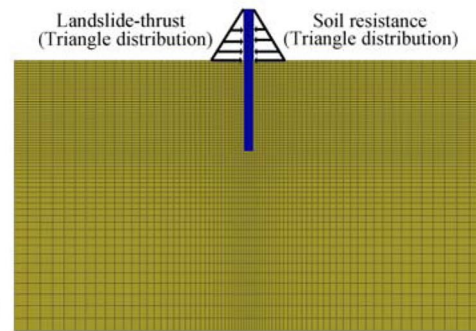
Verification method: We then reckoned the values of earth pressure and soil resistance based on the results of in situ model tests, and substituted them into the three kinds of distribution functions. The equations are shown in Table 4. The



a. Distribution function proposed in this paper



b. Distribution function proposed for clay by Dai



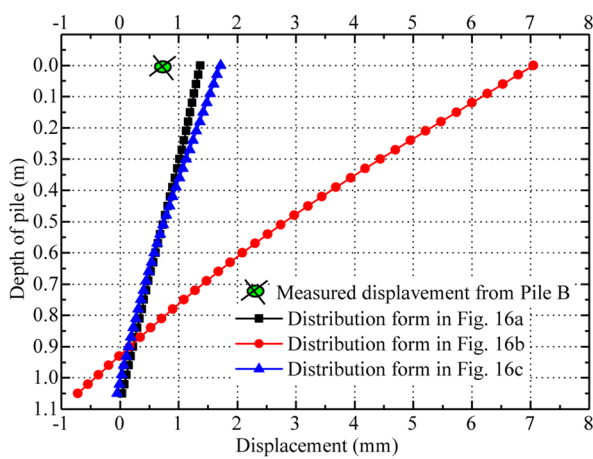
c. Distribution function based on "m" method

Fig. 16 2D numerical model in different distribution forms of lateral loading. **a** Distribution function proposed in this paper. **b** Distribution function proposed for clay by Dai. **c** Distribution function based on "m" method

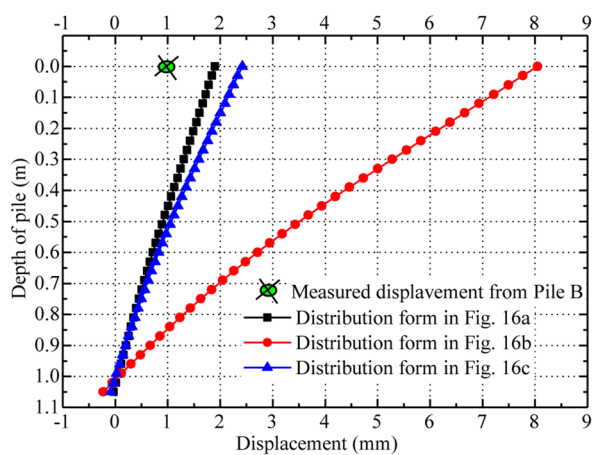
values of earth pressure and soil resistance at the 7th and 11th stages were selected for estimation and were obtained from Fig. 15b. Then, we applied the $ap(z)$ function to the loaded segment of the pile side and $q(z)$ to another side. The contact property of the embedded segment and loess was the same as for the numerical tests above.

Table 4 Loading equation of 2D numerical model

Distribution from	Estimate project	E (kN)	E' (kN)	k or k'	Loading equation
Figure 16a	7th loading	15.19	6.92	$k = 3/5$ $k' = 3/10$	$q(z) = -1.4767 \times 10^6 z^2 + 9.8451 \times 10^5 z + 4.5571 \div 10^4$ $p(z) = -1.4950 \times 10^5 z + 1.3704 \times 10^5$
	11th loading	22.53	11.75	$k = 3/5$ $k' = 3/10$	$q(z) = -2.1906 \times 10^6 z^2 + 1.4602 \times 10^6 z + 6.7593 \times 10^4$ $p(z) = -2.5385 \times 10^5 z + 2.3270 \times 10^5$
Figure 16b	7th loading	15.19	6.92	$k = 7/10$ $k' = 3/10$	$q(z) = 4.9230 \times 10^5 z^2 + 1.6408 \times 10^5 z$ $p(z) = -1.4950 \times 10^5 z + 1.3704 \times 10^5$
	11th loading	22.53	11.75	$k = 7/10$ $k' = 3/10$	$q(z) = 7.3019 \times 10^5 z^2 + 2.4337 \times 10^5 z$ $p(z) = -2.5385 \times 10^5 z + 2.3270 \times 10^5$
Figure 16c	7th loading	15.19	6.92	$k = 2/3$ $k' = 2/3$	$q(z) = 2.7347 \times 10^5 z$ $p(z) = 1.2458 \times 10^5 z$
	11th loading	22.53	11.75	$k = 2/3$ $k' = 2/3$	$q(z) = 4.0562 \times 10^5 z$ $p(z) = 2.1154 \times 10^5 z$

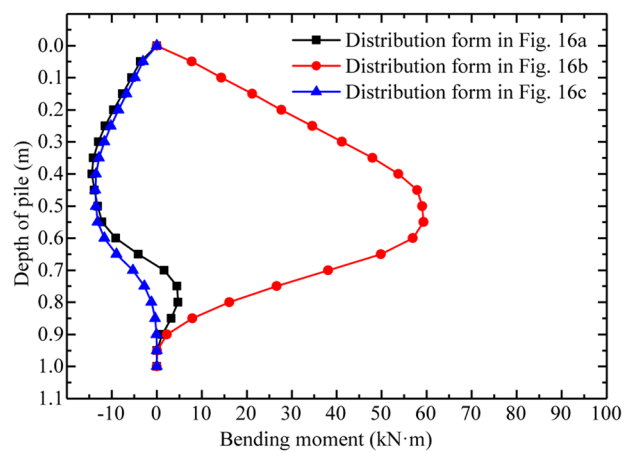


a. Displacement curve ($E = 15.19 \text{ kN}$, $E' = 6.92 \text{ kN}$)

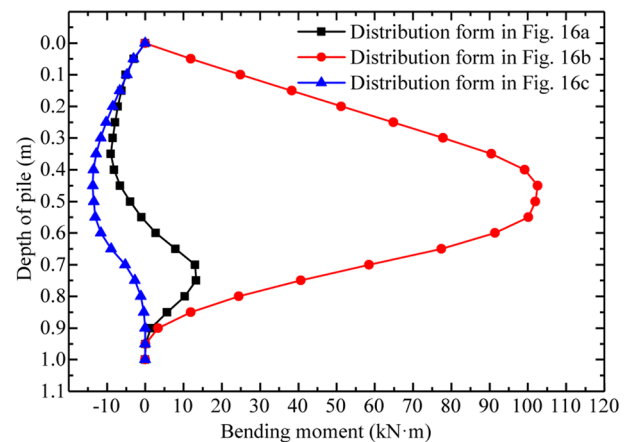


b. Displacement curve ($E = 22.53 \text{ kN}$, $E' = 11.75 \text{ kN}$)

Figure 17 Displacement of piles in different distribution forms but same lateral load. **a** Displacement curve ($E = 15.19 \text{ kN}$, $E' = 6.92 \text{ kN}$). **b** Displacement curve ($E = 22.53 \text{ kN}$, $E' = 11.75 \text{ kN}$)



a. Bending moment ($E = 15.19 \text{ kN}$, $E' = 6.92 \text{ kN}$)



b. Bending moment ($E = 22.53 \text{ kN}$, $E' = 11.75 \text{ kN}$)

Fig. 18 Bending moment of piles in different distribution forms but same lateral load. **a** Bending moment ($E = 15.19 \text{ kN}$, $E' = 6.92 \text{ kN}$). **b** Bending moment ($E = 22.53 \text{ kN}$, $E' = 11.75 \text{ kN}$)

Verification standard: We compared the pile body displacement results produced by the different distribution functions with those of the pile-top of pile B at the corresponding load stages (Fig. 17).

As shown in Fig. 17, under the premise of equivalent earth pressure and soil resistance, different displacement results were calculated using the three distribution forms. The displacements calculated with the distribution form proposed in this study were closest to the measured values.

The bending moments of piles according to the different distribution forms are shown in Fig. 18. Comparing the shapes of the bending moment curves with those of Figs. 10 and 11 shows that the curve calculated using the distribution form of earth pressure and soil resistance proposed in this study was closest to an S-shape. Therefore, according to the displacement and bending moment results, the distribution form proposed by Dai (2002) is not appropriate for loess slopes in northern Shaanxi. The bending moment calculated under the triangular distributed stress showed a D-shape but was still significantly different to the measured bending moment.

Conclusions and suggestions

1. Two groups of tests of in-situ single-row anti-slide pile models were developed from the field direct shear method. The tests confirmed that fully buried single-row anti-slide piles in loess slopes fail due to fracture damage. During the loading process, the piles experienced three stages: non-deformation, effective deformation, and failure.
2. The results obtained from the in-situ model tests and numerical analysis indicate that the earth pressure curve had a parabolic shape with an axis of symmetry located at about 2/3 of the lateral loaded area, while the soil resistance curve had an inverted trapezoidal shape. The resultant force of earth pressure was located within 9/16 to 3/5 of the load-bearing segment, and that of soil resistance was within 3/10 to 2/5.
3. The proposed distribution forms have good applicability to fully buried single-row anti-slide piles installed in loess slopes with a potential sliding surface in northern Shaanxi. This was verified by contrasting the results of the numerical and in-situ tests. Although the parabolic distribution of earth pressure will approximate with trapezoid on pile's displacement and bending moment, it can express the earth pressure attenuation process near the sliding surface reasonably.

Funding This study is supported by Scientific Research Foundation of Graduate School of Southeast University (Grant No. YBPY1926) and

Project of Jiangsu Provincial Transportation Engineering Construction Bureau (CX-2019GC02).

References

- Chen GF, Zou LC, Wang Q, Zhang GD (2020) Pile-spacing calculation of anti-slide pile based on soil arching effect. *Adv Civ Eng* 2020:1–6
- Dai ZH (2002) Study on distribution laws of landslide-thrust and resistance of sliding mass acting on anti-slide piles. *Chin J Rock Mech Eng* 21(4):517–521 ((in Chinese))
- Fan G, Zhang JJ, Qi SC, Wu JB (2019) Dynamic response of a slope reinforced by double-row anti-sliding piles and pre-stressed anchor cables. *J Mt Sci* 16:226–241
- Frank R, Pouget P (2008) Experimental pile subjected to long duration thrusts owing to a moving slope. *Géotechnique* 58:645–658
- Gu M, Kong L, Chen R, Chen Y, Bian X (2014) Response of 1×2 pile group under eccentric lateral loading. *Comput Geotech* 57:114–121
- He GF, Li ZG, Yuan Y, Li XH, Hu LH, Zhang Y (2018) Optimization analysis of the factors affecting the soil arching effect between landslide stabilizing piles. *Nat Resour Model* 31(2): e12148
- Ho IH (2015) Numerical study of slope-stabilizing piles in undrained clayey slopes with a weak thin layer. *Int J Geomech* 15(5):06014025
- Hou TS, Wang XG, Pamukcu S (2015) Geological characteristics and stability evaluation of wanjia middle school slope in wenchuan earthquake area. *Geotech Geol Eng* 34:237–249
- Hull H (1995) Model tests on single piles subjected to lateral soil movement. *Soil and Foundations* 34(4):85–92
- Kang GC, Song YS, Kim TH (2009) Behavior and stability of a large-scale cut slope considering reinforcement stages. *Landslides* 6:263–272
- Li CD, Tang HM, Hu XL, Wang LQ (2013) Numerical modelling study of the load sharing law of anti-sliding piles based on the soil arching effect for erliban landslide, china. *KSCE J Civ Eng* 17:1251–1262
- Li CD, Yan J, Wu J, Lei G, Wang L, Zhang Y (2017) Determination of the embedded length of stabilizing piles in colluvial landslides with upper hard and lower weak bedrock based on the deformation control principle. *Bull Eng Geol Environ* 78:1189–1208
- Li CD, Hu XL, Wang LQ, Ez Eldin MAM (2015) Influence of composite elastic modulus and lateral load pattern on deflection of anti-slide pile head. *J Civ Eng and Manag* 22:382–390
- Li CD, Tang HM, Hu XL, Liu XW, Wang CQ, Liu T, Zhang YQ (2016) Model testing of the response of stabilizing piles in landslides with upper hard and lower weak bedrock. *Eng Geol* 204:65–76
- Li S, Gao H, Xu D, Meng F (2012) Comprehensive determination of reinforcement parameters for high cut slope based on intelligent optimization and numerical analysis. *J Earth Sci* 23:233–242
- Lirer S (2012) Landslide stabilizing piles: experimental evidences and numerical interpretation. *Eng Geol* 149–150:70–77
- Liu HG, Men YM, Cheng LX, Li XC (2011) Model test for the cantilever anti-slide pile of loess landslide. *Advanced in Building Materials, PTS 1–3(261–263):1014–1018*
- Liu XR, Kou MM, Feng H, Zhou Y (2018) Experimental and numerical studies on the deformation response and retaining mechanism of h-type anti-sliding piles in clay landslide. *Environ Earth Sci* 77(5):163
- Nimityongskul N, Kawamata Y, Rayamajhi D, Ashford SA (2018) Full-scale tests on effects of slope on lateral capacity of piles installed in cohesive soils. *J Geotech Geoenviron Eng* 144(1):04017103

- Ozcelik Ersoy C, Yildirim S (2014) Experimental investigation of piles behavior subjected to lateral soil movement. *Teknik Dergi* 25(4):6867–6887
- Pan JL, Goh ATC, Wong KS, Teh CI (2002) Ultimate soil pressures for piles subjected to lateral soil movements. *J Geotech Geoenviron Eng* 128(6):530–535
- Qian TH, Xia WC, Chen F, Ding HX (2011) Model experimental research on anti-sliding characteristics of the frame anti-sliding piles. *Appl Mech Mater* 1446:584–587
- Qiu HJ, Cui P, Regmi AD, Wang YM, Hu S (2017) Slope height and slope gradient controls on the loess slide size within different slip surfaces. *Phys Geogr* 38(4):303–317
- Smethurst JA, Powrie W (2007) Monitoring and analysis of the bending behaviour of discrete piles used to stabilise a railway embankment. *Géotechnique* 57:663–677
- Song YS, Hong WP, Woo KS (2012) Behavior and analysis of stabilizing piles installed in a cut slope during heavy rainfall. *Eng Geol* 129–130:56–67
- Tang HM, Hu XL, Xu C, Li CD, Yong R, Wang LQ (2014) A novel approach for determining landslide pushing force based on landslide-pile interactions. *Eng Geol* 182:15–24
- Vassallo R, Mishra M, Santarsiero G, Masi A (2019) modeling of landslide–tunnel interaction: the Varco d’Izzo case study. *Geotech Geol Eng* 37:5507–5531
- Wang LP, Zhang G (2013) Progressive failure behavior of pile-reinforced clay slopes under surface load conditions. *Environ Earth Sci* 71:5007–5016
- Wang MM, Wu SG, Wang GL (2017) Limit analysis method for active earth pressure on laggings between stabilizing piles. *J Mt Sci* 14(1):196–204
- Xiao SG (2016) A simplified approach for stability analysis of slopes reinforced with one row of embedded stabilizing piles. *Bull Eng Geol Environ* 76:1371–1382
- Xu YL, Guo PP (2020) Disturbance evolution behavior of loess soil under triaxial compression. *Adv Civ Eng* 2020
- Zhang G, Wang LP, Wang YL (2017) Pile reinforcement mechanism of soil slopes. *Acta Geotech* 12:1035–1046
- Zhou CM, Shao W, Van-Westen CJ (2014) Comparing two methods to estimate lateral force acting on stabilizing piles for a landslide in the three gorges reservoir, china. *Eng Geol* 173:41–53
- Zhou SH, Tian ZY, Di HG, Guo PJ, Fu LL (2020) Investigation of a loess-mudstone landslide and the induced structural damage in a high-speed railway tunnel. *Bull Eng Geol Environ* 79(5):2201–2212
- Zomorodian SMA, Dehghan M (2011) Lateral resistance of a pile installed near a reinforced slope. *Int J Phys Model Geotech* 11:156–165